JGR Atmospheres

RESEARCH ARTICLE
10.1029/2023JD038708

Electrification Within Wintertime Stratiform Regions Sampled During the 2020/2022 NASA IMPACTS Field Campaign

Sebastian S. Harkema[1,2], Lawrence D. Carey[1], Christopher J. Schultz[3], Edward R. Mansell[4], Emily B. Berndt[3], Alexandre O. Fierro[5], and Toshi Matsui[6,7]

[1]Department of Atmospheric and Earth Science, University of Alabama in Huntsville, Huntsville, AL, USA, [2]Earth System Science Center, University of Alabama in Huntsville, Huntsville, AL, USA, [3]Earth Science Branch, NASA Marshall Space Flight Center, Huntsville, AL, USA, [4]NOAA/National Severe Storms Laboratory, Norman, OK, USA, [5]Metocean Team, I&E Engineering, BP Exploration and Operating Company, Ltd., Sunbury, UK, [6]Mesoscale Atmospheric Processes Laboratory, NASA Goddard Space Flight Center, Greenbelt, MD, USA, [7]Earth System Science Interdisciplinary Center, University of Maryland, College Park, MD, USA

Key Points:

- Electrification within wintertime stratiform regions were associated with collisions between large non-rimed ice and snow hydrometeors
- For the first time, large-scale electrification was simulated for two nor'easters to provide context to aircraft in-situ observations
- Snow hydrometeors were found to carry more charge density, compared to graupel, in simulated wintertime stratiform regions

Supporting Information:

Supporting Information may be found in the online version of this article.

Correspondence to:

S. S. Harkema,
sebastian.harkema@nasa.gov

Citation:

Harkema, S. S., Carey, L. D., Schultz, C. J., Mansell, E. R., Berndt, E. B., Fierro, A. O., & Matsui, T. (2023). Electrification within wintertime stratiform regions sampled during the 2020/2022 NASA IMPACTS Field Campaign. *Journal of Geophysical Research: Atmospheres*, *128*, e2023JD038708. https://doi.org/10.1029/2023JD038708

Received 15 FEB 2023
Accepted 3 SEP 2023

Abstract Two nor'easter events—sampled during the NASA Investigation of Microphysics and Precipitation for Atlantic Coast-Threatening Snowstorms (IMPACTS) field campaign—were examined to characterize the microphysics in relation to the underlying electrification processes within wintertime stratiform regions. A theoretical model was developed to determine whether accretion or diffusion growth regimes were preferential during periods of greatest electrification. Model simulation with electrification parameterization was used to provide supplemental context to the physical processes of in-cloud microphysics and electrification. The strongest electric fields (i.e., ~80 V m^{-1} at 20 km) during the 2020 NASA IMPACTS deployment was associated with large non-rimed ice crystals colliding with each other. During the 29–30 January 2022 science flight, the NASA P-3 microphysical probe data demonstrated that non-inductive charging was possible off the coastline of Cape Cod, Massachusetts. Later in the science flight, when the NASA P-3 and ER-2 were coordinating with each other, measured electric fields consistently were less than 8 V m^{-1} and electrification was subdued owing to reduced concentrations of graupel and large ice hydrometeors. Altogether, the in-situ observations provide evidence for the non-riming collisional charging mechanism and demonstrates that graupel and supercooled liquid water may not be necessary for weak electrification within wintertime stratiform regions. Model output from simulation of both events suggested that the main synoptic snowbands were associated with elevated hydrometeor snow charge density and electric fields.

Plain Language Summary Cloud particle probe data and numerical weather prediction output were examined to understand the potential electrification processes for two winter storms that impacted the Northeast region of the United States. During the 7 February 2020 event, the greatest observed electrification was associated with pristine ice crystals and large snowflakes in an environment with little to no liquid water and high collision rates between large ice crystals. Electrification was likely during the earlier stages of the 29–30 January 2022 event—via collisions of graupel and ice hydrometeors in the presence of supercooled liquid water—but became subdued later in the flight due to the reduced number of graupel and ice crystals within the cloud structure. The numerical weather prediction model output from the two events suggested that snow carries the most electrical charge in wintertime stratiform regions.

1. Introduction

Cloud electrification must occur on two spatial scales: (a) small scales that electrify individual hydrometeors, and (b) large scales (~5 km) that effectively separates the charges on larger and smaller particles by differential sedimentation. The most widely accepted mechanism for in-cloud electrification is the charge separation that occurs when ice crystals collide with graupel in the presence of supercooled liquid water (SCLW). "Non-inductive" means that the process is not dependent on a pre-existing electric field (Reynolds et al., 1957). Hydrometeor sedimentation serves as the large-scale mechanism responsible for large scale charge separation; whereby relatively fast-falling hydrometeors (i.e., graupel) transfer charge via rebounding collision with ice crystals, and then fall out relative to the crystals (Williams, 1985; Williams & Lhermitte, 1983). Laboratory studies have long supported the importance of charge separation from collisions of graupel with ice crystals when SCLW is present in the initial build-up of electric fields in thunderclouds (e.g., Saunders et al., 2006; Takahashi, 1978). At temperatures

lower than −10°C, hydrometeor collisions leave graupel with either positive or negative charge, depending on the cloud water content (Saunders et al., 2006; Saunders & Peck, 1998; Takahashi, 1978). Laboratory studies have also shown that at warm temperatures between −10°C and −2°C, graupel usually gains positive charge. A so-cold "reversal temperature" may denote the switch between negative and positive charging of graupel, depending on the cloud water content (Jayaratne et al., 1983; Takahashi et al., 1999).

When comparing the riming (i.e., accretion) and completely glaciated environments, Jayaratne et al. (1983) demonstrated that charge transfers on graupel particles were a magnitude less in non-riming environments, non-supersaturated, compared to riming environments. Other laboratory studies have examined non-riming environments and found weak charge transfer (Baker et al., 1987; Caranti et al., 1991; Gaskell & Illingworth, 1980; Saunders et al., 2001). Luque et al. (2016) determined that the charge separated per collisions in non-riming conditions with ice supersaturation were on the same order of magnitude for ice-ice collisions within riming conditions. Using airborne observations, Dye and Bansemer (2019) confirmed previous speculations—from Dye and Willett (2007)—that electric fields (i.e., 10–30 kV m^{-1}) were generated via ice-ice collisions occurring in non-riming environments of stratiform regions of thunderstorms in Florida. Charge separation within this region was inferred from increased/sustained electric fields when ice crystals—growing by deposition—collide without SCLW being present and charging within this region was not dependent on the electrification processes near the melting layer. It should be noted that the non-inductive charging mechanism can occur within riming and non-riming environments. Therefore, and hereafter, whenever riming and non-riming collision mechanism is mentioned, it is with the understanding that it is technically the non-inductive charging mechanism in riming and non-riming environments, respectively.

Studies that have examined the electrification processes in winter weather have predominately focused on storms that develop near the Sea of Japan (e.g., Brook et al., 1982; Kitagawa & Michimoto, 1994; Takahashi et al., 1999; Takeuti et al., 1978; Zheng et al., 2019). Within the United States, most studies have examined winter weather electrification though the use of lightning and radar data sets to provide insight into in-cloud processes or to provide situational awareness for operational forecasters (Harkema et al., 2019, 2020; Market & Becker, 2009; Market et al., 2002, 2006; Rauber et al., 2014; Schultz et al., 2018). Kumjian and Deierling (2015) used dual polarization radar and lightning mapper array measurements to infer microphysical content in regions in which lightning was observed. In most cases, graupel was detected but one case did not suggest graupel, thus suggesting that non-riming electrification might have occurred. Furthermore, Harkema et al. (2022) examined geostationary satellite imagery to infer microphysical changes at cloud top and determined that glaciation and ice collisions and/or gravitational sedimentation occurred prior to lightning initiation when the surface experienced snowfall.

Rust and Trapp (2002) examined the electric field and diagnosed charge structure of six winter nimbostratus clouds using in-situ balloon observations. Three of the cloud structures were associated with snowfall at the surface and charging aloft. Furthermore, wintertime stratiform regions generally had regions of positive charge over regions of negatively charged hydrometeors (Rust & Trapp, 2002; Schultz et al., 2018). During the NASA Investigation of Microphysics and Precipitation for Atlantic Coast-Threatening Snowstorms (IMPACTS; McMurdie et al., 2022) field campaign, the Lightning Instrument Package (LIP; Bateman et al., 2007; Koshak et al., 2006; Mach et al., 2020; Mach & Koshak, 2007) was deployed on the NASA ER-2. Schultz et al. (2021) found that electric field measurements—sampled at an altitude of ∼20 km—from NASA IMPACTS were as high as 80 V m^{-1} above non-lightning producing winter clouds and were horizontally co-located with in-situ observations with periods of ice supersaturation and enhancements of SCLW. Electrification was also observed in non-riming environments and provides support to the non-riming collision mechanism (Dye & Bansemer, 2019). Furthermore, Schultz et al. (2021) determined that these enhanced electric fields coincide with observed in-cloud electrification as evident in differential reflectivity depolarization streaks (e.g., Kumjian, 2013). However, Schultz et al. (2021) did not quantitatively examine their results with respect to ice crystal growth regimes, hydrometeor collision rates, and the underlying ice crystal concentrations collected during the field deployments.

The availability of NASA IMPACTS field campaign observations provides an unparalleled opportunity to investigate the role of SCLW on the electrification processes within heavy-banded snowfall structures. Understanding these electrification processes within winter storms also has implications toward a larger understanding of electrification within stratiform regions associated with severe convective weather. Therefore, the questions this study addressed were: (a) Is it possible to determine if an environment is primarily associated with either the riming or non-riming collision mechanisms from in-situ microphysical probe data? (b) How important is the

presence of SCLW and graupel for electrification within wintertime stratiform regions? (c) Is graupel necessary to produce any electrification within wintertime stratiform regions? The objectives of this manuscript are.

1. Develop a theoretical model that can differentiate non-riming (i.e., diffusion) and riming (i.e., accretion) ice crystal growth regime environments using NASA IMPACTS microphysical probe data.
2. Quantitatively examine the above theoretical model in relationship to observed SCLW and the presence of graupel and relate them to the electric field measurements from LIP.
3. Simulate the two nor'easter events using a numerical weather prediction model that uses an explicit electrification parameterization.

2. Data and Methods

2.1. Lightning Instrument Package

The seven rotating vane electric field mills mounted on the body of the NASA ER-2 aircraft during the NASA IMPACTS field campaign were employed to determine the electric fields in the x-, y-, and z-directions as well as the electric field produced by charge on the aircraft itself. These electric field mills are collectively known as the LIP. Rapid changes of the electric field usually indicate the presence of lightning. In controlled laboratory settings, these field mills were shown to be sensitive to within a precision of ± 1.9 V m^{-1} to 1.1 MV m^{-1} (Mach et al., 2009). Between the 2020 and 2022 NASA IMPACTS deployments, the LIP hardware was updated to increase electric field sensitivity down to 1 V m^{-1} resolution, reduce power consumption, and minimize data storage footprint on the host aircraft (Mach et al., 2022). It should be noted that all electric field measurements were taken at the sampling altitude of the ER-2 (i.e., ∼20 km or ∼50 hPa).

2.2. The P-3 Orion In Situ Probes

In-situ microphysical instrumentation were attached to the body of NASA's P-3 Orion for the NASA IMPACTS field campaign and generally sampled cloud structure between −18°C and −4°C. The Rosemount icing detector (RICE) was one of these instruments and provided observations of SCLW and is associated with a noise level of about 0.002 g m^{-3} (Heymsfield & Miloshevich, 1989). RICE does not directly measure the amount of SCLW but provides a signal that it exists. The RICE probe oscillates ice-free at a standby frequency of 40 kHz and decreases when SCLW accretes on the probe. When 0.5 mm of ice is accumulated on the probe, it is heated for 5 s followed by a 5–10 s cool down period so that SCLW can again accrete on the probe (Bansemer et al., 2020). The Droplet Measurement Technologies' Cloud Droplet Probe (CDP) from the University of North Dakota was also mounted on the P-3 and can directly estimate liquid water content (LWC) from droplet size and concentration and has been shown to have less bias in LWC measurements compared to other instrumentation in mixed phase and low liquid water environments (Cober et al., 2001; Delene & Poellot, 2020; Lance et al., 2010).

The Stratton Park Engineering Company's two-dimensional stereo probe (2D-S) and Hawkeye Cloud Particle Imager (CPI) provide direct quantitative values to the particles within the cloud (Bansemer et al., 2020). The 2D-S is an imager that consists of two diode arrays with a spatial resolution of 10 μm per pixel and thus provide shadow images of particles in the vertical and horizontal orientation. As a result, the 2D-S imagery can be used to estimate particle size distribution (PSD) characteristics (e.g., total hydrometeor collision rate). Thus, the examination of the PSD provides additional context to the microphysics-electrification processes within stratiform regions/winter storms (Dye & Bansemer, 2019). The Hawkeye CPI also provides imagery of particles but with higher spatial resolution of 2.3 μm per pixel (Bansemer et al., 2020). This high-resolution imagery can capture individual hydrometeors and provide a context to hydrometeor type (e.g., column, dendrite, rimed ice crystal), and therefore does not estimate PSD characteristics. It should also be mentioned that a 10 s rolling mean was applied to all P-3 observation measurements.

2.3. Theoretical Accretional Versus Diffusional Growth

The riming collision mechanism is dependent on the fact that graupel, ice crystals, and SCLW must coexist in the mixed-phase region of a cloud; however, how important is SCLW to electrification processes? Riming collision mechanism occurs—in part—because ice crystals grow via collection of SCLW droplets (Equation 1):

$$\left(\frac{dm}{dt}\right)_{\text{accretion}} = \overline{E} M \pi R^2 v \tag{1}$$

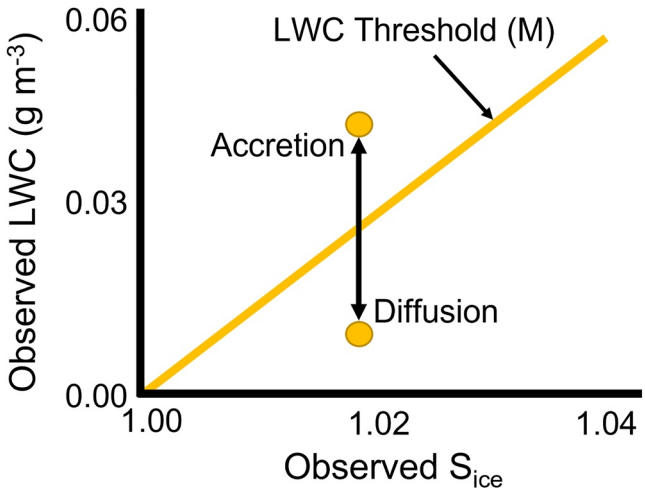

Figure 1. Schematic that highlights the linear relationship between the theoretical liquid water content (LWC) threshold and observed ice supersaturation. The mass of hydrometeors with a positive or negative deviation in observed LWC off the yellow line would be growing faster via accretion or diffusion growth processes, respectively.

where the left-hand side of Equation 1 represents the mass growth rate of an ice crystal via accretion (riming), $\bar{E}$ is the collection efficiency, M is LWC, R is the ice particle radius, v is the ice particle fall speed (Rogers & Yau, 1989). In contrast, water vapor is used to grow ice crystals via diffusion (Equation 2):

$$\left(\frac{dm}{dt}\right)_{\text{diffusion}} = \frac{4\pi C(S_i - 1)}{\left[\left(\frac{L_s}{R_v T} - 1\right)\frac{L_s}{KT} + \frac{R_v T}{e_i D}\right]} \quad (2)$$

where the left-hand side of Equation 2 represents the mass growth rate of an ice crystal via diffusion, C is the capacitance (shape) parameter, S_i is supersaturation with respect to ice, L_s is the latent heat of sublimation, R_v, is the gas constant of water vapor, T is temperature, K is the coefficient of thermal conductivity of air, e_i is saturated vapor pressure of ice, D is the coefficient of diffusion of water vapor in air. It should be noted that Equation 2 neglects the kinematic effects on ice crystal growth via diffusion (Rogers & Yau, 1989).

Jensen and Harrington (2015) developed a single-particle growth model to examine the growth characteristics caused by vapor growth and riming and builds on previous laboratory studies that examined environments with different levels of LWC (Takahashi et al., 1991; Takahashi & Fukuta, 1988). Figure 1 in Jensen and Harrington (2015) hypothesized that a LWC threshold could separate preferred accretional and diffusional ice crystal growth regimes. This theoretical LWC threshold would provide insight into the extent that SCLW plays in the electrification process via riming collision (Reynolds et al., 1957) and the non-riming collision (Dye & Bansemer, 2019) mechanisms. Although it is assumed within this analysis, change in ice crystal growth regime does not necessarily mean that the change in charge separation is at the same limit as that differentiating particle growth. As a result, the theoretical LWC threshold can be calculated by setting Equations 1 and 2 equal to each other and solving for M (i.e., LWC):

$$M = \frac{4C(S_i - 1)}{\overline{E}R^2 v\left[\left(\frac{L_s}{R_v T} - 1\right)\frac{L_s}{KT} + \frac{R_v T}{e_i D}\right]} \quad (3)$$

Note the linear relationship between the M (i.e., LWC threshold) and S_i (i.e., ice supersaturation). Collection efficiency ($\bar{E}$) is a function of ice particle size, the cloud droplet size, and the relative velocity between them. Furthermore, the velocity (v) is a function of the size and shape of the ice particles as well as the environment conditions, while the shape parameter (C) is related to the major and minor axes of the particle. When S_i is <1 (i.e., environment is subsaturated with respect to ice), Equation 3 produces a negative value for M which has no physical meaning. Therefore, negative values of M values were set to zero before any analysis. It was assumed that any ice crystal with a shape parameter could be associated with a circular cross-sectional area. For example, a regular hexagon plate ice crystal was assumed to be a circle with some depth. This is an adequate assumption given that this is a simple theoretical model that ignores kinematic effects. Figure 1 is a schematic that demonstrates the linearity of the derived LWC threshold when compared to ice supersaturation for the accretion versus diffusion growth regimes and is based on general ice crystal shape in Table 1 that were used to parameterize the theoretical LWC model. More specifically, it demonstrates that for two observed LWC values (i.e., one on either side of the LWC threshold) associated with the same ice supersaturation, the ice crystal growth regime will be different based on the deviation from the theoretical LWC threshold value. Therefore, an observed LWC greater (less) than this theoretical LWC threshold value would favor ice crystal mass growth in the accretion (diffusion) regime.

Table 1
Ice Crystal Habits—And Associated Characteristics—That Were Used in the Theoretical Ice Crystal Growth Regime Model

Ice crystal habit	C-axis (C)	A-axis (A)	Modeled shape
Needle	15	1	Needle
Plate/Dendrite	1	9	Thin plate
Column	5	2	Column
Graupel	2	3	Oblate spheroid

Note. The C- and A-axis are related to the prism and basal face of the ice crystals. For example, for a needle ice crystal, the C-axis is related to the prism length and for a plate ice crystal, the A-axis is related to the radius of the basal face.

2.4. Ice Hydrometeor Collision Rate

Another key component of non-inductive charging is hydrometeor collision rate, which can be used as a proxy for small-scale charge separation

between hydrometeors. For a given PSD, the total collision rate can by calculated using Equation 4 (Dye & Bansemer, 2019):

$$C_T = \frac{1}{2} \sum_D \sum_d C_{D,d} \tag{4}$$

where $C_{D,d}$ is the collision rate between large (i.e., D) and small (i.e., d) particles over the entire PSD and can be calculated using Equation 5 (Dye & Bansemer, 2019).

$$C_{D,d} = \frac{\pi}{4} N_D N_d E (D + d)^2 (V_D - V_d) \tag{5}$$

where N_x and V_x are the concentration and terminal fall speeds of the large and small particles, respectively; E is the collision efficiency; and $(D + d)^2$ is the cross-sectional area.

Using the methodology from Dye and Bansemer (2019), total collision rate was calculated using Equation 4 with an assumed perfect collision efficiency (i.e., $E = 1$). An assumed perfect collision efficiency represents a best-case scenario connecting the charging processes that may have occurred in the environment that was being sampled by the P-3. The terminal velocity of the hydrometers was estimated following the methodology described in Heymsfield and Westbrook (2010). Terminal velocities are a function of area ratio, hydrometeor diameter and mass, and environmental characteristics (e.g., density of air), all of which could be derived from P-3 observational data. Furthermore, the crystal with sector-like branching mass-diameter relationship was used to estimate ice hydrometer mass for the terminal velocity calculations (Mitchell, 1996; Pruppacher & Klett, 1978). Several ice particle types from Mitchell (1996) were tested but the crystal with sector-like branching produced the most realistic terminal fall speeds with respect to the NASA IMPACTS microphysical probe data.

2.5. Numerical Weather Prediction Modeling

To provide additional context to the NASA IMPACTS observations, the NASA Unified Weather Research and Forecasting with the electrification parameterization (NU-WRF-ELEC; Fierro et al., 2013; Mansell et al., 2005; Peters-Lidard et al., 2015; Skamarock & Klemp, 2008) was used to produce simulations for the two nor'easters. Seven different model configurations for the 7 February 2020 event were quantitatively compared to observed reflectivity structures via contour frequency by altitude diagram analysis. This sensitivity testing including changing the planetary boundary layer, longwave/shortwave radiation, and convective schemes. Figure 2 demonstrates the final model spatial domain configurations for the 7 February 2020 and 29–30 January 2022 cases, respectively.

For the 7 February 2020 simulation, the innermost domain had a grid spacing of ~333 m centered over New York State; in contrast; the 29–30 January 2022 simulation's innermost domain had a grid spacing of 1,000 m centered over New England (Table 2). The latter simulation has a coarser inner domain grid spacing owing to the larger area of interest demonstrated by the aircraft flight lines (Figure 2c). Table 2 also contains additional information regarding parameterizations used in the model configuration.

The NU-WRF-ELEC simulations used the National Severe Storms Laboratory (NSSL) two-moment bulk microphysics scheme (Mansell et al., 2010), which predicts the mass mixing ratio and number concentration for six hydrometeor types (i.e., droplets, rain, ice crystals, snow, graupel, and hail). Graupel and hail further have predicted mean particle density. All hydrometeor classes have predicted charge density through various charging processes and mass transfers between species (Mansell et al., 2005). Inductive charging were parameterized via Mansell et al. (2005) and non-inductive charging was parameterized using the modified Saunders and Peck (1998) scheme (Mansell et al., 2010). Furthermore, charge can be distributed and separated throughout the system via the continuity equation for charge on hydrometeors (Equation 6; Mansell et al., 2005):

$$\frac{\partial \rho_n}{\partial t} = -\nabla \cdot (\rho_n V) + \nabla \cdot (K_h \nabla \rho_n) + \frac{\partial (V_{t,n} \rho_n)}{\partial z} + S_n \tag{6}$$

where the left-hand side represents the net charge budget tendency on a given hydrometer type, and the right-hand terms represent advection of charge transport (including resolved turbulent eddies), subgrid turbulent mixing, hydrometeor sedimentation, and local sink and source terms. These terms are not explicitly found within the

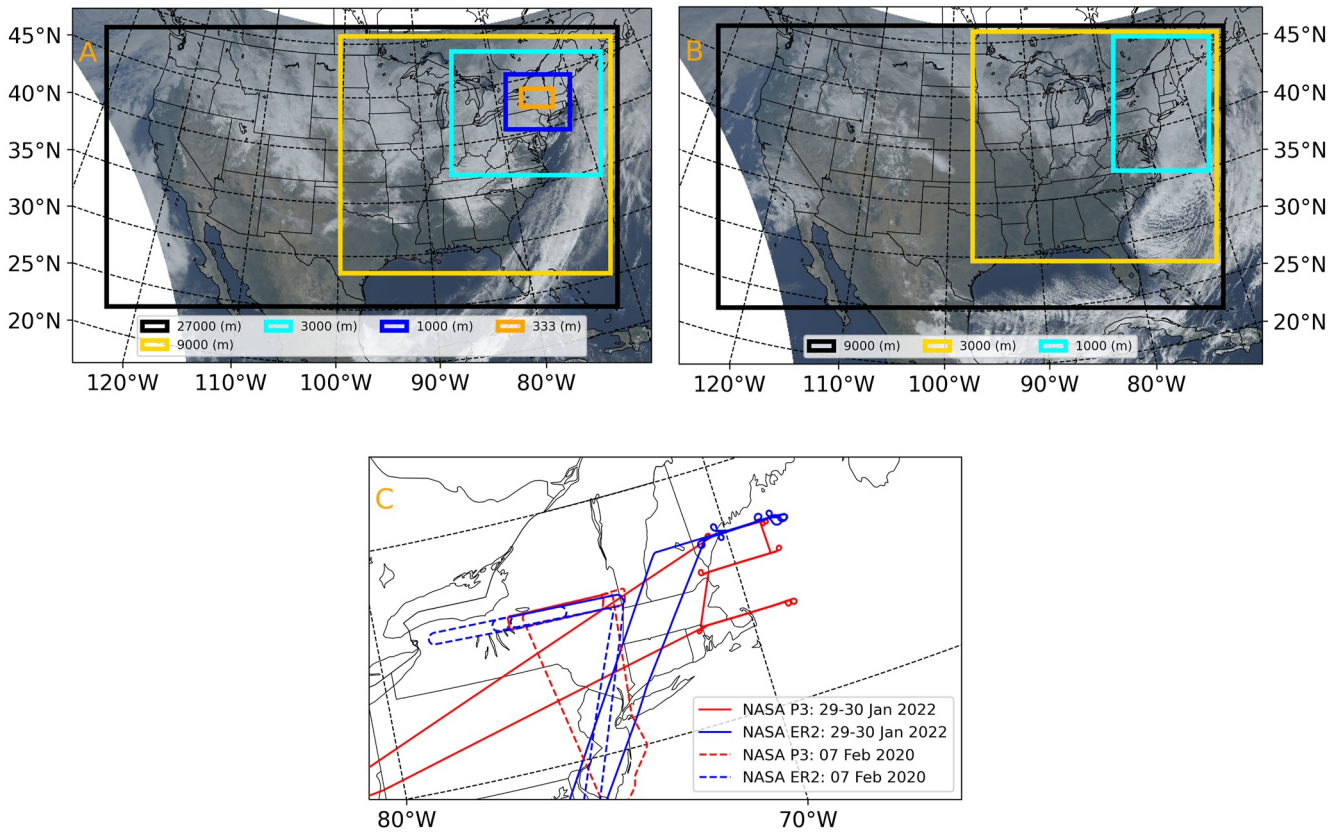

Figure 2. Configuration of the NU-WRF-ELEC model-simulation for the (a) 7 February 2020 and (b) 29–30 January 2022 NASA IMPACTS science flights. The colored boxes represent the individual domains for each of the simulations. The background is Geostationary Operational Environmental Satellite—East true color imagery at 1801 UTC on 7 February 2020 and 29 January 2022, respectively. (c) The flight tracks for the ER-2 (blue) and P-3 (red) for the respected science flights.

WRF-ELEC model output. Brothers et al. (2018) expanded Equation 6 in their model simulations and determined that lightning deposition, sedimentation, and non-inductive charging tendencies contributed most to the charge budget of simulated summer convective storms. The bulk lightning discharge scheme (adapted from Ziegler and MacGorman (1994)) was implemented for both simulations (Fierro et al., 2013). Essentially, this lightning parameterization produces a cylindrical discharge when the electric field exceeds a critical threshold (Dwyer, 2003). Following the methods of Ziegler et al. (1991), a screening layer was applied to all clear air/cloud boundaries. It should be mentioned that WRF-ELEC sets charging (i.e., non-inductive and inductive) to zero in environments with a rime accretion rate <0.1 g m^{-2} s^{-1} (i.e., low LWC environments; Mansell et al., 2005, 2010; Saunders & Peck, 1998). As a result, WRF-ELEC cannot explicitly resolve the charging via the non-riming collision mechanism.

Table 2
Summary of Key Physical and Numerical Parameterizations of the Innermost Domain for the Two Winter Storm Cases

Parameters/case	7 February 2020	29–30 January 2022
ΔX (m)	~333	1,000
N_Z	70	70
N_X x N_Y	1,000 × 565	1,000 × 1,402
dt (s)	~0.37	~1.67
Boundary Layer Scheme	YSU	YSU
Radiation Scheme	RRTMG	RRTMG
Microphysics Scheme	NSSL two-moment	NSSL two-moment
Land Surface Model	Noah	Noah
Initial-Boundary Conditions	HRRR (v3)	HRRR (v4)

Note. The variables Δ*X*, N_Z, N_X *x* N_Y, and *dt* are the horizontal grid spacing, number of vertical layers, number of grid points in the zonal and meridional directions, and computational time step, respectively.

3. Analysis

3.1. Riming and Non-Riming Case: 7 February 2020

The NASA ER-2 and P-3 were sampling a rain-to-snow transition region in New York State—in a coordinated race-track pattern—that was associated with a rapidly deepening cyclone (Figure 2a). Lightning flashes were observed during the 7 February 2020 snowstorm but occurred outside of sampling domain for the science flights (not shown). During this science flight, LIP was measuring electric fields as high as 80 V m^{-1} which were the highest recorded during the 2020 NASA IMPACTS field deployment

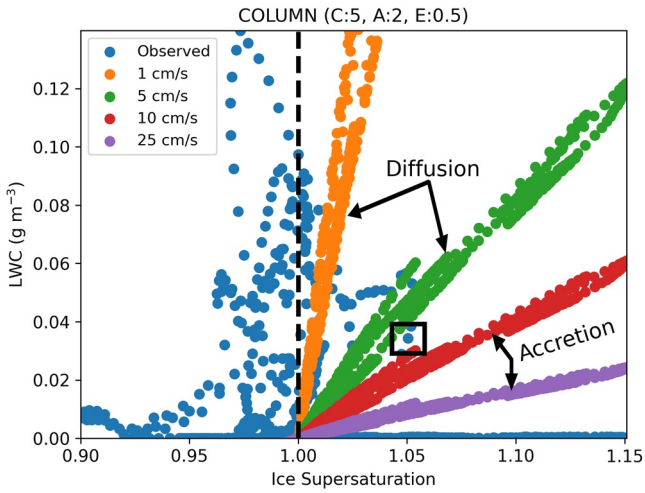

Figure 3. Observed ice supersaturation and liquid water content (LWC) values (blue dots) between 1530 and 1545 UTC on 7 February 2020. The black box represents the potential environment of interest. Assuming a column ice particle with a radius and length of 0.85 and 2.13 mm, respectively and a collection efficiency of 0.5. The non-blue colored dots represent the theoretical LWC threshold based on observed ice supersaturation at four different terminal fall speeds. Diffusional growth will be favored with lower fall speeds and accretional growth with higher fall speeds with respect to the black boxed environment. The vertical black dashed line represents 100% ice supersaturation and provides insight into sublimation (ice supersaturation $< 100\%$) and diffusion (ice supersaturation $\geq 100\%$) environments.

(Schultz et al., 2021). Schultz et al. also determined that some enhancements in electric fields were associated with non-riming environments while others showed no enhanced electric fields. As a result, this case provided an ideal scenario for investigating the electrification complexities associated with both riming and non-riming environments.

Using NASA IMPACTS microphysical probe data from 1530 to 1545 UTC on 7 February 2020, the theoretical LWC threshold for a single column ice crystal with a radius and length of 0.85 and 2.13 mm, respectively, was calculated at four different fall speeds (Figure 3). In an environment with a LWC of 3×10^{-2} g m^{-3} and an ice supersaturation of 1.05 (i.e., the observation within the black box), the column ice crystal could be growing in either a diffusion or accretion dominant growth regime depending on the ice crystal terminal fall speed. At lower fall speeds (i.e., 1 and 5 cm s^{-1}), the modeled hydrometeor would be in a diffusion dominant growth region with respect to the black boxed environment in Figure 3. In contrast, at higher fall speeds (i.e., 10 and 25 cm s^{-1}) the accretion growth regime would be favored for the specific modeled hydrometeor as the observed LWC has a positive deviation off the theoretical LWC threshold. From an electrification perspective, the faster falling column ice crystal would theoretically be charging—in that instant in time—via the riming collision mechanism because the column ice crystal was collecting more SCLW and colliding with smaller crystals. Whereas the non-riming collision mechanism would be favored at lower fall speeds because the column ice crystal was growing faster via diffusion at that instant in time. Although it is assumed in this analysis, it should be noted that any changes in ice crystal growth regime may not be at the same limit with regards to changes in charge separation.

Between 1530 and 1545 UTC on 7 February 2020, the P-3 was flying at an altitude of approximately 3.6 km while sampling a rain-to-snow transition region. The sampled environmental temperature in the rain (snow) region was approximately −6°C (−10°C). During this period, the CPI onboard the P-3 showed that ice hydrometeors where heavily rimed at the beginning of the flight leg and became less rimed (i.e., more pristine) as the aircraft traversed west across the rain-to-snow transition region (Figures 4a and 4b). The theoretical ice crystal growth regime model for a plate ice crystal match with the CPI observations while the P-3 transitioned between riming to non-riming environments when the collection efficiency was assumed to be one (Figure 4c). See the supplemental material to see how the theoretical model output changes when different collection efficiencies were used. The shading in the background represents deviation (orange = negative, blue = positive) from the theoretical LWC threshold (i.e., M) based on the calculated LWC from CDP (lime green line), the median mass-weighted ice hydrometeor radius from 2D-S (orange line), and ice supersaturation (red line) at various terminal fall speeds between 0 and 100 cm s^{-1}. Figure 4c also contains z-direction electric field measurements from LIP (solid black line) and an adjusted electric field to account for spatiotemporal differences between the ER-2 and P-3 (dashed black line). Between 1530 and 1535 UTC, the CDP LWC values were as high as 0.14 g m^{-3} but generally hovered between 0.02 and 0.1 g m^{-3}. The decrease in CDP LWC after 1535 UTC coincides with the P-3 crossing the rain region to the snowy region of the system. During this time, the microphysical probe data estimated an overall increase in median mass-weighted ice hydrometeor radius from 0.74 to 2.02 mm and z-direction electric fields where on the order of 10 V m^{-1} or less. Enhancements in ice supersaturation can occur during periods with relatively high LWC. As a result, the theoretical model suggests that ice crystals will be growing faster via diffusion at lower terminal fall speeds even when LWC was relatively high. The theoretical model estimated with reasonable confidence that accretion was the dominant growth regime for the median ice crystal because of the elevated LWC values. In contrast, the theoretical model estimated that the dominant growth regime between 1535 and 1545 UTC was diffusion except at higher terminal fall speeds and generally matches the CPI imagery (Figures 4b and 4c). Furthermore, the theoretical model indicated several periods of time where it had little-to-no confidence in either accretion or diffusion being the dominant growth regime at the various modeled fall speeds (i.e., all white background throughout the y-axis model fall speeds; Figure 4c). More specifically, there were entire periods when the theoretical model was

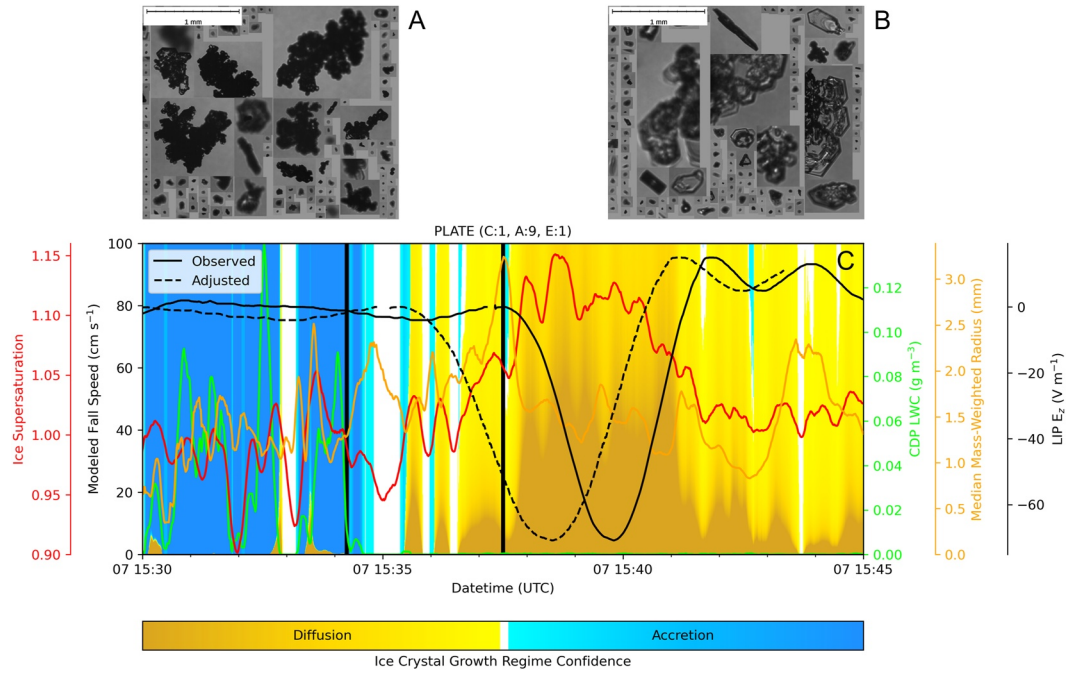

Figure 4. (a) Rimed ice crystals (1534:15 UTC) and (b) Pristine ice crystals (1537:30 UTC) observed by the cloud particle imager on 7 February 2020 (times denoted by thick vertical lines on panel c); (c) Modeled variation of a modeled plate ice crystal with a collection efficiency of one, C-axis and A-axis of one and nine, respectively. The primary *y*-axis represents modeled terminal fall speeds of a modeled plate ice crystal. The ice crystal growth regime based on the theoretical liquid water content (LWC), observed LWC (lime green line) and ice supersaturation (red line), and median mass-weighted hydrometeor radius (orange line). Black lines represent LIP observations while the dashed line represents the spatiotemporally adjusted electric fields to account for offsets between the NASA ER-2 and P-3.

not defining a dominant growth regime for any modeled fall speed (e.g., 1535 UTC). Interestingly, this time was associated with derived CDP LWC values $\ll 0.01$ g m^{-3} and ice supersaturation as low as 0.94. As a result, the theoretical model could be suggesting that this timeframe was associated with an environment that was favoring sublimation compared to accretion and diffusion. This becomes more evident when the collection efficiency was decreased (see the supplemental material). *Z*-direction electric fields were between $\pm$12 V m^{-1} and suggested that weak electrification could have been possible during periods of sublimation (Figure 4c). Even when accounting for the spatiotemporal offsets of the P-3 and ER-2, the largest LIP *z*-direction electric fields magnitudes (i.e., $\sim$70 V m^{-1}) were associated with this region of relatively low LWC and pristine ice crystals. It is important to note, however, that the P-3 pass is at one level, which may not necessarily be representative of the whole column.

The transition from riming to non-riming environments can also be seen in the hydrometeor collision rates (Figure 5). During periods with enhanced SCLW, the RICE frequency dropped below the 40 kHz standby frequency and was collocated with the greatest overall collision rates associated with hydrometeors with a diameter $\geq$20 μm (thin black line). At 1533:37 UTC, the collisions associated with small hydrometeors between 20 and 100 μm and all other hydrometeors (i.e., $D \geq 20$ μm) account for 98.9% of all collisions (thick vertical black line). This is demonstrated by the separation between the total collision rates when only considering certain hydrometeor diameter as noted by the separation between the black and orange lines between 1530 and 1535 UTC (Figure 5). Starting at 1535 UTC, the collision rates stabilized to less than 146 m^{-3} s^{-1} and was associated with a RICE frequency of 40 kHz (i.e., no SCLW). Furthermore, the total collision rate between all hydrometeors was dominated by larger ice hydrometeors. At 1538:30 UTC, time of strongest measured adjusted electric field, the total collision rate between ice hydrometeors $\geq$250 and $\geq$475 μm accounted for 81.4% and 66.5% of the total ice hydrometeor collision rate, respectively (thick vertical black line; Figure 5). At this time, the environment was associated with a total collision rate of 142 m^{-3} s^{-1} and was dominated by large ice crystals colliding with each other. Therefore, the largest electric field measured during the 2020 NASA IMPACTS field campaign was associated within pristine ice crystal environment without an obvious riming process. This is supported via CPI imager data and the theoretical ice crystal growth regime model (Figures 4b and 4c).

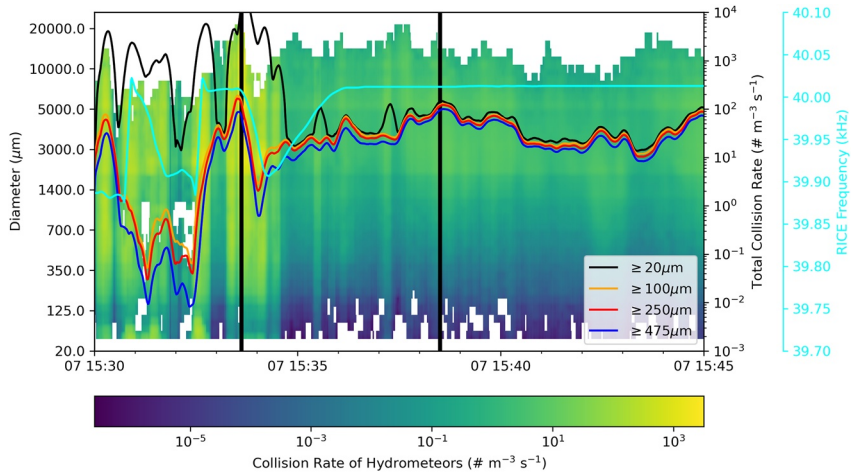

Figure 5. Calculated hydrometeor collision rates (multicolored lines) and RICE frequency (cyan line) between 1530 and 1545 UTC on 7 February 2020. The ordinate (*y*-axis) physically represents the binned ice crystal diameters derived from the 2DS data. Background represents the calculated total collision rate associated with a particular binned ice crystal diameter. The vertical black lines represent 1533:37 and 1538:30 UTC, respectively.

At 1430 UTC on 7 February 2020, the NU-WRF-ELEC simulation was associated with a pocket of elevated electric fields and hydrometeor charge densities near the rain-to-snow transition region (Figure 6). The simulation had a deep region of ice supersaturation between 900 and 400 hPa yet this region was not coincident with stronger vertical motions. The simulation developed a saturated nearly isothermal layer between the surface and 800 hPa. Simulated electric field vertical profile peaked at 700 hPa and exceeded 800 V m^{-1}. This peak in electric field coincided with a local maximum in vertical motions. The net and individual hydrometeor charge densities were very weak, with magnitudes less than 10^{-11} C m^{-3} except for a localized peak in droplet charge. The droplet charge is still quite weak and likely was produced by the screening layer parameterization. Even though the vertical profile was below freezing, charged rain hydrometeors likely exist in the profile because they were advected from the above freezing side of the rain-to-snow transition region. Furthermore, it should be mentioned that the

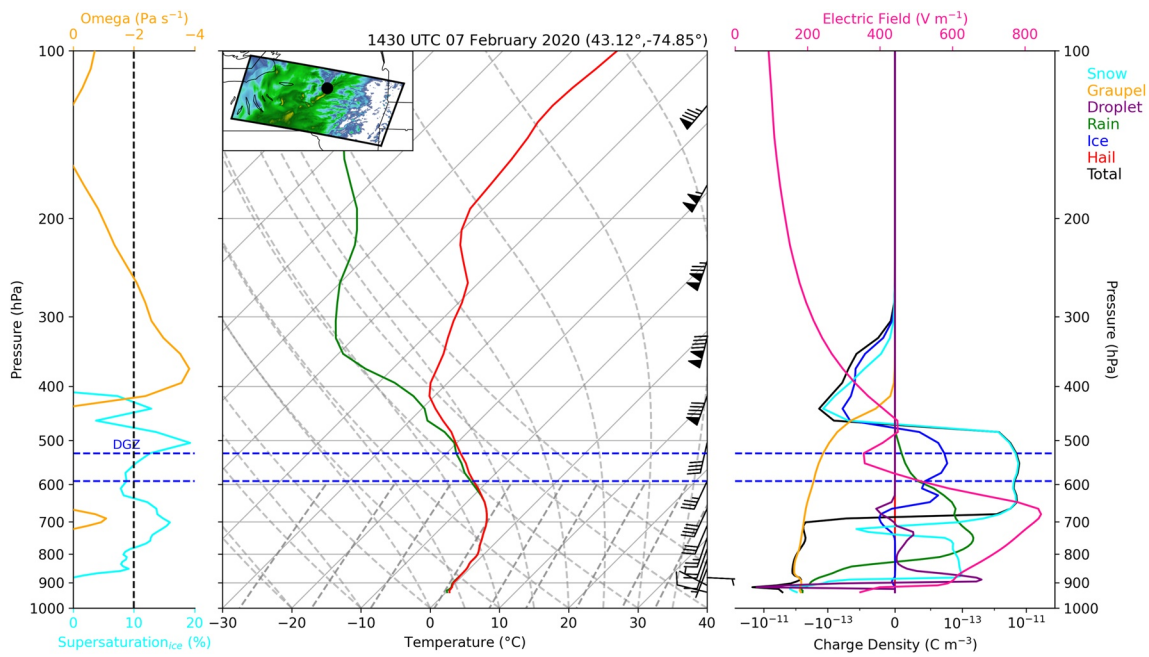

Figure 6. NU-WRF-ELEC simulated profile at 43.12°N, −74.85°W at 1430 UTC on 7 February 2020. The inset map includes simulated composite reflectivity (AGL > 2500 m) at 1430 UTC.

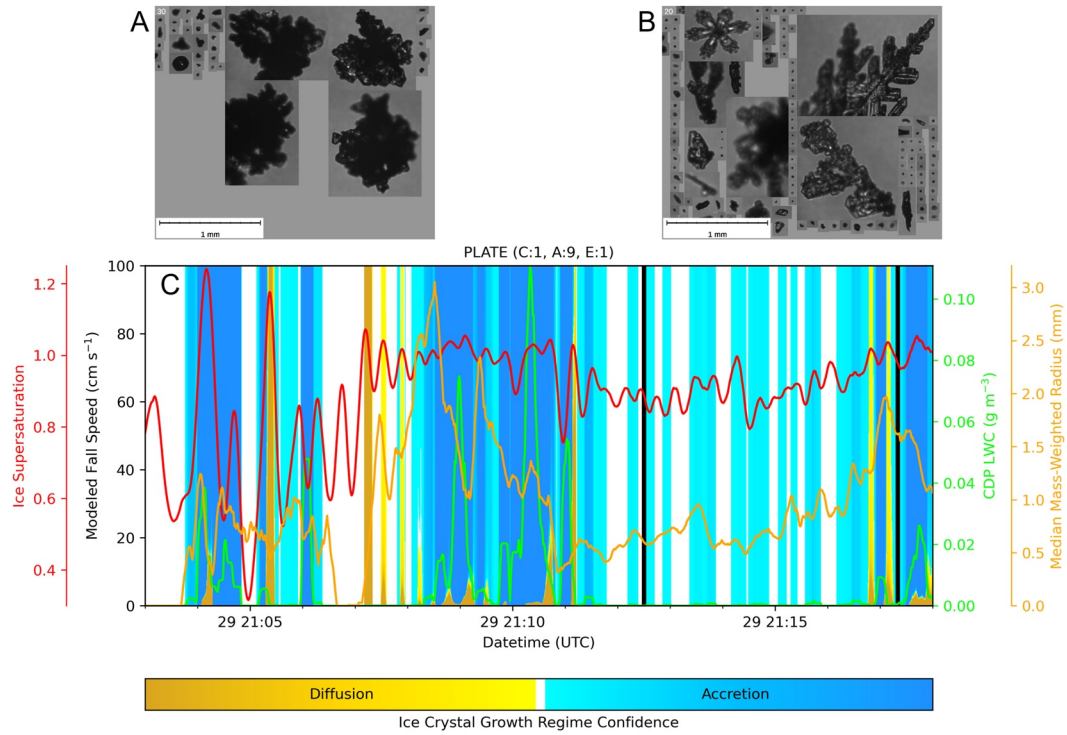

Figure 7. (a) Graupel (2112:30 UTC) and (b) moderately rimed ice crystals (2117:20 UTC) observed by the cloud particle imager on 29 January 2022; (c) Modeled variation of a modeled plate ice crystal with a collection efficiency of one, C-axis and A-axis of one and nine, respectively. The primary *y*-axis represents modeled terminal fall speeds of a modeled plate ice crystal. The ice crystal growth regime based on the theoretical liquid water content (LWC), observed LWC (lime green line), ice supersaturation (red line), and median mass-weighted hydrometeor radius (orange line).

ER-2 was not sampling this location at the time; however, simulated electric field was 82 V m^{-1} at 54 hPa which was the approximate pressure at which the ER-2 was sampling.

3.2. Large Societal Impact Case: 29–30 January 2022

The late January 2022 nor'easter produced copious amounts of snowfall with Plymouth, Massachusetts accumulating over 61 cm of snowfall (Figure 2b). Although thundersnow was highly anticipated by forecasters and the public for this event, none was reported or observed. As a result, this event served as a null case to investigate the underlying microphysics to account for the lack of lightning within nor'easters that are associated with large societal impacts. From 2013 to 2354 UTC on 29 January 2022, the NASA P-3 was performing cross-sections sampling the snowband near Cape Cod, Massachusetts and later off the coastline of Portsmouth, New Hampshire. The NASA ER-2 had a delayed take-off because of airport conditions at Pope Army Airfield not meeting safety guidelines, which also limited the number of coordinated P-3 and ER-2 passes. From 0030 to 0147 UTC on 30 January 2022, the NASA ER-2 and P-3 flights had four coordinated legs and sampled the snowband off the Portland, Maine coastline.

Between 2103 and 2118 UTC, the CPI indicated a rimed environment (Figures 7a and 7b). Graupel hydrometeors were pronounced at the beginning of this timeframe and heavily rimed sectored plates became more abundant toward the end. The theoretical ice crystal growth regime suggested that accretion growth would be greater than diffusional growth for much of this leg (Figure 7c). At 2110:20 UTC, a peak CDP LWC of 0.11 g m^{-3} was chiefly associated with accretion (i.e., dark blue background; Figure 7). In contrast, between 2111:32 and 2116:43 UTC, the CDP LWC values where less than 0.01 g m^{-3} and, consequently, the theoretical model was weakly favoring an accretion growth regime. This aligns with the CPI observations during this period where the highest LWC values were associated with graupel hydrometeors, while the period of relatively low LWC values were primarily associated with moderately rimed ice crystals. Furthermore, the median mass-weighted diameter was less than 2-mm during this period of relatively low LWC. Unlike the period highlighted in Figure 4, nearly

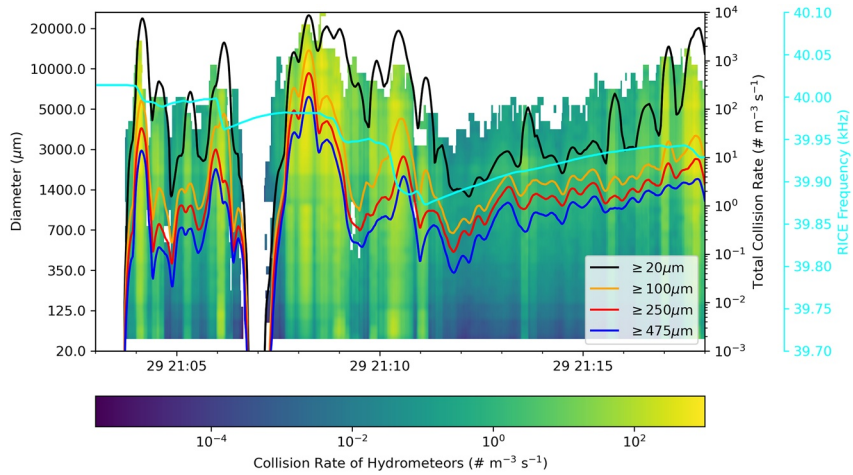

Figure 8. Calculated hydrometeor collision rates (multicolored lines) and RICE frequency (cyan line) between 2103 and 2118 UTC on 29 January 2022. The ordinate (*y*-axis) physically represents the binned ice crystal diameters derived from the 2D-S data. Background represents the calculated total collision rate associated with a particular binned ice crystal diameter.

the entire time within Figure 7 is subsaturated with respect to ice (i.e., ice supersaturation < 1). As a result, the theoretical model had little-to-no confidence that accretion or diffusion was the dominant growth regime (i.e., all white background throughout the *y*-axis model fall speeds; Figure 7) in regions that were associated with low LWCs and subsaturated with respect to ice at the various modeled fall speeds. This suggests that the ice crystals were sublimating faster than they were growing from accretion. Between 2104 and 2118 UTC (i.e., nearly the whole time of Figures 7 and 8), the vibrating frequency of RICE never reached the 40 kHz standby vibrating frequency (Figure 8), providing further evidence that SCLW existed during this flight leg. Periods with elevated LWC values coincided with the highest total collision rates (Figures 7 and 8). Between 2111 and 2117 UTC, the total collision rate never exceeded 1,000 m^{-3} s^{-1}, which was a result of smaller hydrometeor size and lower concentrations. Although this leg had no coordination between the P-3 and ER-2 flight, the microphysical probe data supported the potential for electrification within this snowband via the riming collision mechanism (i.e., collision and presence of graupel, ice particles, and SCLW; Figures 7 and 8).

Even though there was no coordination between the P-3 and ER-2 between 2013 and 2354 UTC on 29 January 2022, the microphysical probe data do support the potential for electrification via the riming collision mechanism. At 2112 UTC, the P-3 was sampling off the coast of Cape Code, Massachusetts. At the same time, the NU-WRF-ELEC simulation had the main synoptic snowband shifted north and offshore by approximately 100 km compared to what was observed (not shown). At 2112 UTC and south of the Maine coastline, NU-WRF-ELEC simulated a layer of enhanced ice supersaturation from 900 to 440 hPa (Figure 9). The vertical profile was also associated with weak vertical motions with values >-1 Pa s^{-1} and no clear upward motion within the dendritic growth zone. Furthermore, NU-WRF-ELEC indicated a stronger surface inversion with below freezing temperatures throughout the profile. The electrification parameterization produced an extremely weak charge structure with maximum charge density magnitudes less than 10^{-12} C m^{-3}, one order of magnitude weaker compared to the 7 February 2020 simulation. The electric field still appreciably exceeded typical fair-weather magnitudes and exceeded 120 V m^{-1} throughout much of the lower troposphere (Figure 9). NU-WRF-ELEC also simulated an electric field of 62 V m^{-1} at ∼54 hPa within this vertical profile. Altogether, NU-WRF-ELEC suggested the potential for electrification within the main synoptic snowband prior to the sampling period of the ER-2.

The P-3 and ER-2 had two coordinated legs between 0030 and 0100 UTC on 30 January 2022 off the coast of Maine. The two legs sampled the same region but sampled two different microphysical environments. During the first leg (i.e., 0030–0045 UTC; Figure 10a), CPI observed both pristine and heavily rimed ice hydrometeors with the latter becoming more dominant toward the second half of the flight leg (not shown). The mean median mass-weighted radius was 1.03 mm and was associated with a maximum CDP LWC of 3×10^{-2} g m^{-3} (Figure 10a). For a modeled plate ice crystal, the theoretical growth regime model suggested that sublimation was the dominate regime between 0032 and 0035 UTC as the environment was subsaturated with respect to ice and associated with low LWC (Figure 10a). After 0040 UTC, the theoretical model suggested with high

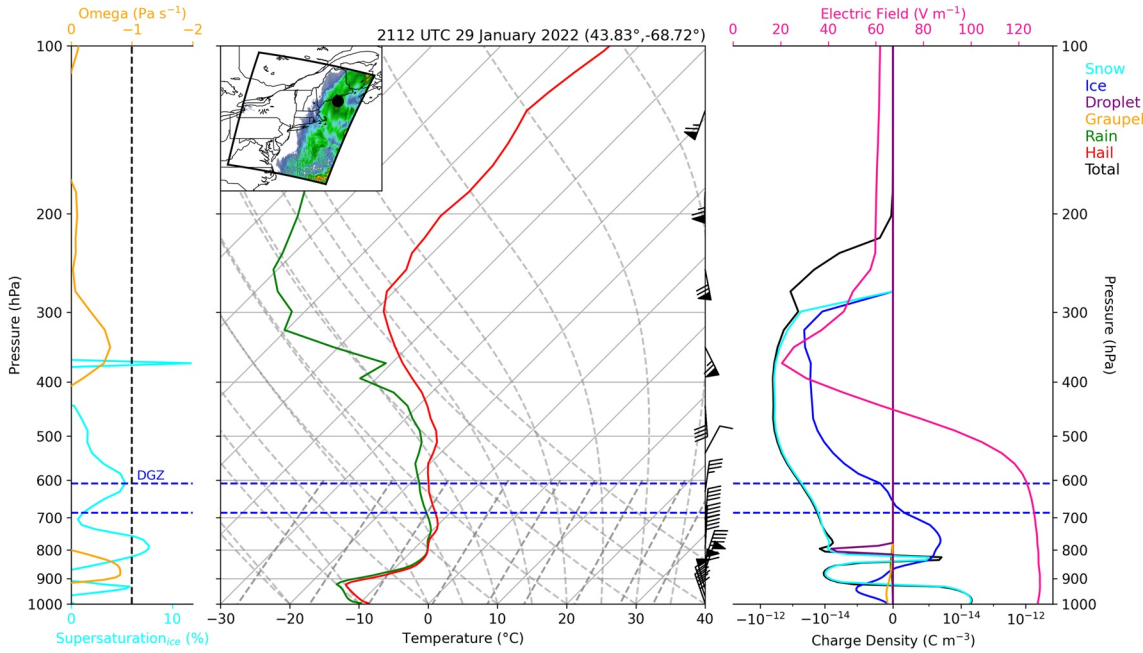

Figure 9. NU-WRF-ELEC simulated profile at 43.83°N, −68.72°W at 2112 UTC on 29 January 2022. The inset map includes simulated composite reflectivity (AGL > 500 m) at 2112 UTC.

confidence that accretion was the dominant growth regime. The second leg (i.e., 0045–0100 UTC; Figure 10b) was associated with a smaller mean median mass-weighted radius (i.e., 0.44 mm) and a higher maximum LWC (i.e., 0.15 g m^{-3}). Like that in Figures 4 and 7, little-to-no confidence of accretion or diffusion growth regimes (i.e., all white background throughout the *y*-axis model fall speeds; Figures 10a and 10b) were associated with an environment with low LWC and subsaturated with respect to ice. As a result, these periods of time were likely associated with ice crystals shrinking via sublimation. During these periods of sublimation, *z*-direction electric fields varied in value between −3 to 1.5 V m^{-1}. The main differences between the two flight legs were caused by the lower concentration of large ice particles and increased concentration of SCLW droplets. Between 0045 and 0100 UTC on 30 January 2022, total collision rates associated with hydrometeors ≥100 μm never exceeded 70 m^{-3} s^{-1}. Even though SCLW was present, electrification was negligible during these two flight legs because of the reduced number of ice crystals and/or graupel particles. This is evident in LIP *z*-direction adjusted electric field as it chiefly varied between −5 and 8 V m^{-1} throughout these two legs (Figures 10a and 10b).

4. Discussion

The largest electric fields measured during the 2020 NASA IMPACTS field campaign were associated with collisions between large ice particles within a non-riming environment; thus, supporting the non-riming collisional mechanism for in-situ charging (Dye & Bansemer, 2019). Calculated total collision rates were less than 200 m^{-3} s^{-1} at peak electrification measured by LIP (i.e., 80 V m^{-1}) on 7 February 2020; in contrast, Dye and Bansemer (2019) calculated that collision rates exceeded 500 m^{-3} s^{-1} during periods of strong electrification within a Florida stratiform region. The collision rates within this study, however, were predominately associated with larger ice hydrometeors; whereas collisions associated with smaller hydrometeors dominated the collision rate within Dye and Bansemer (2019). Furthermore, the collision rates at peak electrification were for a single flight leg and may not represent the full depth of the cloud. It should also be noted the Dye and Bansemer (2019) included observations from six electric field mills within the cloudy region while the LIP mills sampled the electric field above cloud top.

The vast majority of laboratory studies that have examined electrification mechanisms have focused on collisional charging between riming graupel and ice/snow crystals (e.g., Brooks et al., 1997; Jayaratne et al., 1983; Saunders et al., 2006; Saunders & Peck, 1998; Takahashi, 1978). The in-situ observations of Takahashi et al. (1999) showed the electric charge carried by graupel pellets and ice crystals within thunderstorm and non-thunderstorm cases for

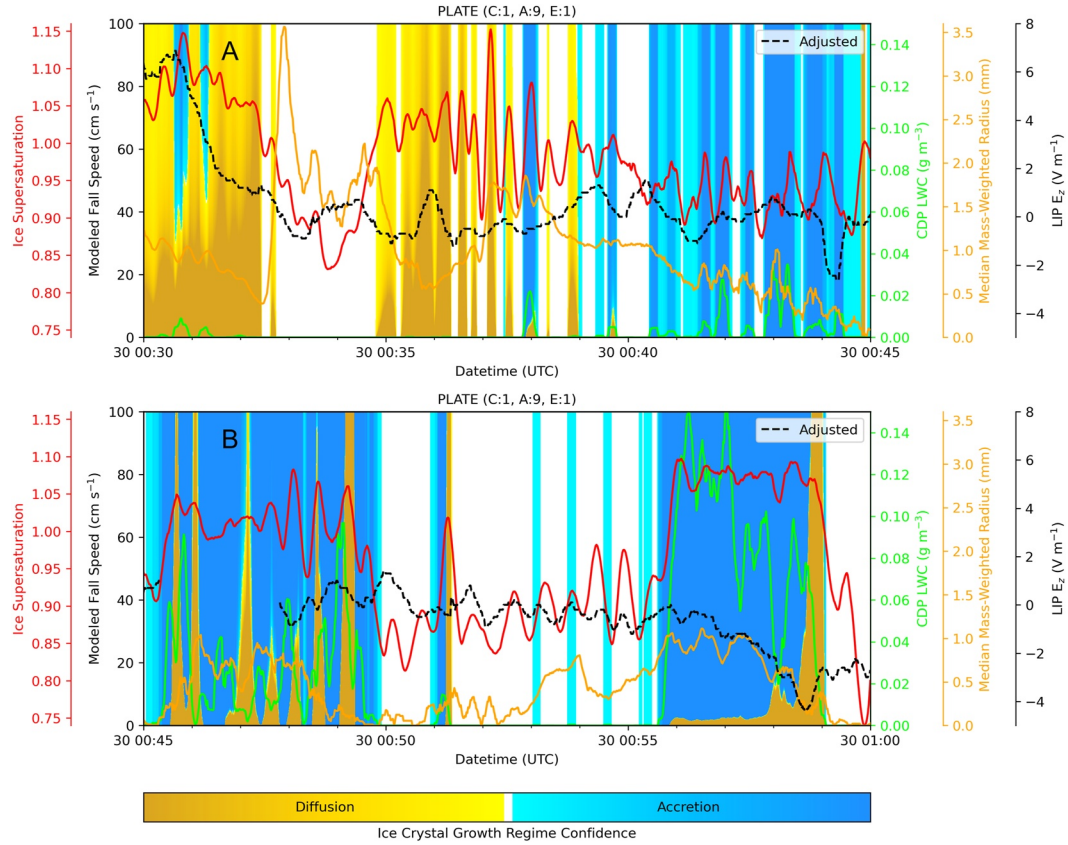

Figure 10. Modeled variation of a modeled plate ice crystal with a collection efficiency of one, C-axis and A-axis of one and nine, respectively. The primary *y*-axis represents modeled terminal fall speeds of a modeled plate ice crystal. The ice crystal growth regime based on the theoretical liquid water content (LWC), observed LWC (lime green line), ice supersaturation (red line), and median mass-weighted hydrometeor radius (orange line) between (a) 0030 and 0045 UTC and (b) 0045 and 0100 UTC on 30 January 2022. The black dashed line represents the spatiotemporally adjusted LIP electric fields to account for offsets between the NASA ER-2 and P-3.

varying PSD spectra. Although not explicitly discussed in their research, their Figure 16 suggests that ice crystals have the potential for carrying more charge compared to graupel (of similar size) especially when the diameters of the hydrometeors are smaller than 0.7 mm. This result generally matches the physically based simulation from the NU-WRF-ELEC, which highlighted that graupel may not always be the dominant charge carrier with wintertime stratiform regions. Additionally, it could be a result of bulk classification of graupel as generally characterized by larger, fully rimed particles, and thus a failure to produce sufficient rimed particles to drive electrification.

Figures 6 and 9 suggest the NU-WRF-ELEC simulations produced measurable electric fields (i.e., >100 V m^{-1}) for the 7 February 2020 and 29–30 January 2022 cases. Furthermore, 54 hPa simulated electric fields in those vertical profiles were approximately 80 and 60 V m^{-1}, respectively. These magnitudes were comparable to observed electric fields on 7 February 2020 (Schultz et al., 2021). When examining the charging processes (i.e., non-inductive and inductive) within Figures 6 and 9 locations, both the non-inductive and inductive charge separation rates were several magnitudes lower compared to the individual and total charge densities within the vertical profiles. This suggests that the charges in the vertical profiles (Figures 6 and 9) were not locally generated. Furthermore, it should be noted that the ER-2 was not sampling the locations of the vertical profiles at their respected times. However, both vertical profiles do support the notion that the main synoptic snowbands were electrified in both cases but far from supporting lightning initiation.

Fierro et al. (2013) simulated a winter storm in the Great Lakes region, which yielded electric field magnitudes generally less than 50 V m^{-1} within the cloud structure and thus no lightning. Similar results were produced within the NU-WRF-ELEC simulations within this study. The largest simulated electric field magnitudes generated within snowfall regions in the 7 February 2020 and 29–30 January 2022 simulations were 11.6 and

18.3 kV m^{-1}, respectively—much greater than the 0.1–0.8 kV m^{-1} of the selected profiles. The maximum electric field in snowy regions on 7 February 2020 (i.e., 11.6 kV m^{-1}) was associated with a graupel charge density on the order of 10^{-10} C m^{-3} and a maximum vertical velocity of 7.2 m s^{-1}. In contrast, the graupel charge density were on the order of 10^{-11} C m^{-3} and a maximum vertical velocity of 0.56 m s^{-1} for the 29–30 January 2022 simulation. These suggests that enhanced electric fields may be possible in convective and non-convective snowfall regions. To the authors knowledge, this work is the first showing that substantial electrification can be produced for snowstorms with electrification parameterization but also not enough for lightning. This suggests potential of utilizing models similar to NU-WRF-ELEC to augment our understanding of the electrification processes within snowstorms (Harkema et al., 2019; Market et al., 2002; Schultz, 1999). It should also be mentioned that the individual hydrometeor PSD within bulk microphysics scheme (e.g., NSSL) likely do not match with those from observations from the NASA IMPACTS field campaign. As a result, any electrification comparisons between the numerical model output and observations must be placed within the context that there were likely inherent differences between the observed and simulated hydrometeors. Analysis would be warranted to compare the NSSL PSD and those observed during the NASA IMPACTS field campaign but is beyond the scope of this project.

5. Conclusions

Both laboratory studies and observations shows that charge separation can occur in summertime stratiform regions via non-riming ice-ice collisions in summertime stratiform regions with charge generated generally not depending on the melting zone (Dye & Bansemer, 2019). Therefore, this study examined two nor'easters sampled during the NASA IMPACTS field campaign using aircraft data to gain a better understanding of the electrification processes occurring within wintertime stratiform regions. More specifically, this study examined data from microphysical probes mounted onboard the NASA P-3 and established connections to the theoretical electrification process (e.g., riming and non-riming collision mechanisms and ice crystal growth regimes) and electric field measurements from LIP onboard the NASA ER-2 aircraft. A theoretical model was developed for this analysis that could quantify accretion (i.e., riming) and diffusion (i.e., non-riming) ice crystal growth regimes. NU-WRF-ELEC simulations supplemented the aircraft observations and theoretical model to provide additional context to the overall charge structure within wintertime stratiform regions sampled during the NASA IMPACTS field campaign.

The chief goal of this study was to develop a method that can be used to quantify charge separated regions associated with non-inductive charging within riming and non-riming environments. This work focused on the importance of SCLW, graupel and hydrometeor collision rates with respect to the underlying electrification potential within wintertime stratiform regions. The main takeaways from this work are.

1. Accretion (riming) and diffusion (non-riming) growth regimes can be identified using aircraft microphysical probe data and can be related to the non-inductive charging mechanism in riming and non-riming environments.
2. Lightning within snowfall occurred outside the sampling range of the aircraft or did not occur during the 7 February 2020 and 29–30 January 2022 cases, respectively. The strongest electric fields from the 2020 NASA IMPACTS field deployment were associated with a non-riming environment and the collision rates were dominated by collisions between large ice crystals. As a result, we infer that electric fields at 20 km within wintertime stratiform regions can be generated by the non-riming collision mechanism.
3. Weak electrification was simulated using NU-WRF-ELEC and vertical profiles of mean hydrometeor charge density were examined. Electric fields as high as 800 V m^{-1} and 128 V m^{-1} were simulated within the synoptic snowbands during the 7 February 2020 and 29–30 January 2022 cases, respectively. The modeled charging processes (i.e., non-inductive and inductive) were only active for conditions of riming, which suggests that riming may be only a sufficient but not necessary condition for appreciable charge separation.

Overall, understanding the microphysical processes within winter storms provides insight into the electrification processes within stratiform regions. Furthermore, the NU-WRF-ELEC simulations did not produce any lightning discharges within snowfall in either simulation. As a result, a follow-up study will examine the potential of using NU-WRF-ELEC to simulate a mid-latitude cyclone associated with lightning within snowfall. Furthermore, it would be advantageous to perform Lagrangian analysis to track charged hydrometeors to fully understanding the physical processes that may impact the charge structure in these wintertime stratiform regions.

Data Availability Statement

NASA IMPACTS data used within this study can be freely obtained online from the NASA Global Hydrology Resource Center Distributed Active Archive Center, Huntsville, Alabama, USA (McMurdie et al., 2019). The HRRR data used to initialize the NU-WRF simulations can be obtained via NOAA's Amazon Web Service (Benjamin et al., 2016; Blaylock et al., 2017; accessed via https://noaa-hrrr-bdp-pds.s3.amazonaws.com/index.html). NU-WRF-ELEC software are available in https://nuwrf.gsfc.nasa.gov/software.

Acknowledgments
This work is part of a larger investigation of electrified snowfall that is directly supported through NASA's Future Investigators in NASA Earth and Space Science and Technology (FINESST) program 80NSSC20K1623. Additionally, this work was also supported by Dr. Tsengdar Lee of NASA's Research and Analysis Program, Weather and Atmospheric Dynamics Focus Area, as part of the Short-term Prediction Research and Transition (SPoRT) Center at Marshall Space Flight Center and supported through the NASA-UAH Cooperative agreement 80MSFC22M0004. The authors would also like to thank the NASA Center for Climate Simulation for allotting computational time on the Discover Supercomputer to run the two simulations. Lastly, the authors want to thank Jim Dye and the two anonymous reviewers for providing valuable insight and suggestions regarding the analysis of the theoretical microphysical model and NU-WRF-ELEC.

References

Baker, B., Baker, M. B., Jayaratne, E. R., Latham, J., & Saunders, C. P. R. (1987). The influence of diffusional growth rates on the charge transfer accompanying rebounding collisions between ice crystals and soft hailstones. *Quarterly Journal of the Royal Meteorological Society*, *113*(478), 1193–1215. https://doi.org/10.1002/qj.49711347807

Bansemer, A., Delene, D., Heymsfield, A. J., O'Brien, J., Poellot, M. R., Sand, K., & Sova, G. (2020). NCAR particle probes IMPACTS. In *Dataset available online from the NASA global Hydrology Resource Center DAAC*. https://doi.org/10.5067/IMPACTS/PROBES/DATA101

Bateman, M. G., Stewart, M. F., Podgorny, S. J., Christian, H. J., Mach, D. M., Blakeslee, R. J., et al. (2007). A low-noise, microprocessor-controlled, internally digitizing rotating-vane electric field mill for airborne platforms. *Journal of Atmospheric and Oceanic Technology*, *24*(7), 1245–1255. https://doi.org/10.1175/JTECH2039.1

Benjamin, S. G., Weygandt, S. S., Brown, J. M., Hu, M., Alexander, C. R., Smirnova, T. G., et al. (2016). A North American hourly assimilation and model forecast cycle: The rapid refresh. *Monthly Weather Review*, *144*(4), 1669–1694. https://doi.org/10.1175/MWR-D-15-0242.1

Blaylock, B. K., Horel, J. D., & Liston, S. T. (2017). Cloud archiving and data mining of High-Resolution Rapid Refresh forecast model output. *Computers and Geosciences*, *109*(C), 43–50. https://doi.org/10.1016/j.cageo.2017.08.005

Brook, M., Nakano, M., Krehbiel, P., & Takeuti, T. (1982). The electrical structure of the hokuriku winter thunderstorms. *Journal of Geophysical Research*, *87*(C2), 1207–1215. https://doi.org/10.1029/JC087iC02p01207

Brooks, I. M., Saunders, C. P. R., Mitzeva, R. P., & Peck, S. L. (1997). The effect on thunderstorm charging of the rate of rime accretion by graupel. *Atmospheric Research*, *43*(3), 277–295. https://doi.org/10.1016/S0169-8095(96)00043-9

Brothers, M. D., Bruning, E. C., & Mansell, E. R. (2018). Investigating the relative contributions of charge deposition and turbulence in organizing charge within a thunderstorm. *Journal of the Atmospheric Sciences*, *75*(9), 3265–3284. https://doi.org/10.1175/JAS-D-18-0007.1

Caranti, G. M., Avila, E. E., & Ré, M. A. (1991). Charge transfer during individual collisions in ice growing from vapor deposition. *Journal of Geophysical Research*, *96*(D8), 15365–15375. https://doi.org/10.1029/90JD02691

Cober, S. G., Isaac, G. A., Korolev, A. V., & Strapp, J. W. (2001). Assessing cloud-phase conditions. *Journal of Applied Meteorology and Climatology*, *40*(11), 1967–1983. https://doi.org/10.1175/1520-0450(2001)040<1967:ACPC>2.0.CO;2

Delene, D., & Poellot, M. (2020). *UND cloud microphysics impacts*. NASA Global Hydrology Resource Center DAAC. https://doi.org/10.5067/IMPACTS/MULTIPLE/DATA101

Dwyer, J. R. (2003). A fundamental limit on electric fields in air. *Geophysical Research Letters*, *30*(20). https://doi.org/10.1029/2003GL017781

Dye, J. E., & Bansemer, A. (2019). Electrification in mesoscale updrafts of deep stratiform and Anvil Clouds in Florida. *Journal of Geophysical Research: Atmospheres*, *124*(2), 1021–1049. https://doi.org/10.1029/2018JD029130

Dye, J. E., & Willett, J. C. (2007). Observed enhancement of reflectivity and the electric field in Long-Lived Florida Anvils. *Monthly Weather Review*, *135*(10), 3362–3380. https://doi.org/10.1175/MWR3484.1

Fierro, A. O., Mansell, E. R., MacGorman, D. R., & Ziegler, C. L. (2013). The implementation of an explicit charging and discharge lightning scheme within the WRF-ARW model: Benchmark simulations of a continental squall line, a tropical cyclone, and a winter storm. *Monthly Weather Review*, *141*(7), 2390–2415. https://doi.org/10.1175/MWR-D-12-00278.1

Gaskell, W., & Illingworth, A. J. (1980). Charge transfer accompanying individual collisions between ice particles and its role in thunderstorm electrification. *Quarterly Journal of the Royal Meteorological Society*, *106*(450), 841–854. https://doi.org/10.1002/qj.49710645013

Harkema, S. S., Berndt, E. B., Mecikalski, J. R., & Cordak, A. (2022). Advanced baseline imager cloud-top trajectories and properties of electrified snowfall flash initiation. *Weather and Forecasting*, *36*(6), 2289–2303. https://doi.org/10.1175/WAF-D-21-0003.1

Harkema, S. S., Berndt, E. B., & Schultz, C. J. (2020). Characterization of snowfall rates, totals, and snow-to-liquid ratios in electrified snowfall events identified by the geostationary lightning mapper. *Weather and Forecasting*, *35*(2), 673–689. https://doi.org/10.1175/WAF-D-19-0126.1

Harkema, S. S., Schultz, C. J., Berndt, E. B., & Bitzer, P. M. (2019). Geostationary lightning mapper flash characteristics of electrified snowfall events. *Weather and Forecasting*, *34*(5), 1571–1585. https://doi.org/10.1175/WAF-D-19-0082.1

Heymsfield, A. J., & Miloshevich, L. M. (1989). Evaluation of liquid water measuring instruments in cold clouds sampled during FIRE. *Journal of Atmospheric and Oceanic Technology*, *6*(3), 378–388. https://doi.org/10.1175/1520-0426(1989)006<0378:EOLWMI>2.0.CO;2

Heymsfield, A. J., & Westbrook, C. D. (2010). Advances in the estimation of ice particle fall speeds using laboratory and field measurements. *Journal of the Atmospheric Sciences*, *67*(8), 2469–2482. https://doi.org/10.1175/2010JAS3379.1

Jayaratne, E. R., Saunders, C. P. R., & Hallett, J. (1983). Laboratory studies of the charging of soft-hail during ice crystal interactions. *Quarterly Journal of the Royal Meteorological Society*, *109*(461), 609–630. https://doi.org/10.1002/qj.49710946111

Jensen, A. A., & Harrington, J. Y. (2015). Modeling ice crystal aspect ratio evolution during riming: A single-particle growth model. *Journal of the Atmospheric Sciences*, *72*(7), 2569–2590. https://doi.org/10.1175/JAS-D-14-0297.1

Kitagawa, N., & Michimoto, K. (1994). Meteorological and electrical aspects of winter thunderclouds. *Journal of Geophysical Research*, *99*(D5), 10713–10721. https://doi.org/10.1029/94JD00288

Koshak, W. J., Mach, D. M., Christian, H. J., Stewart, M. F., & Bateman, M. G. (2006). Retrieving storm electric fields from aircraft field mill data. Part II: Applications. *Journal of Atmospheric and Oceanic Technology*, *23*(10), 1303–1322. https://doi.org/10.1175/JTECH1918.1

Kumjian, M. (2013). Principles and applications of dual-polarization weather radar. Part III: Artifacts. *Journal of Operational Meteorology*, *1*(21), 265–274. https://doi.org/10.15191/nwajom.2013.0121

Kumjian, M. R., & Deierling, W. (2015). Analysis of thundersnow storms over Northern Colorado. *Weather and Forecasting*, *30*(6), 1469–1490. https://doi.org/10.1175/WAF-D-15-0007.1

Lance, S., Brock, C. A., Rogers, D., & Gordon, J. A. (2010). Water droplet calibration of the Cloud Droplet Probe (CDP) and in-flight performance in liquid, ice and mixed-phase clouds during ARCPAC. *Atmospheric Measurement Techniques*, *3*(6), 1683–1706. https://doi.org/10.5194/amt-3-1683-2010

Luque, M. Y., Bürgesser, R., & Ávila, E. (2016). Thunderstorm graupel charging in the absence of supercooled water droplets. *Quarterly Journal of the Royal Meteorological Society*, *142*(699), 2418–2423. https://doi.org/10.1002/qj.2834

Mach, D. M., Bateman, M., & Schultz, C. (2022). *Lightning instrument package (LIP) IMPACTS*. NASA Global Hydrology Resource Center DAAC. https://doi.org/10.5067/IMPACTS/LIP/DATA101

Mach, D. M., Bateman, M. G., & Schultz, C. J. (2020). *Lightning instrument package (LIP) IMPACTS*. NASA Global Hydrology Resource Center DAAC. https://doi.org/10.5067/IMPACTS/LIP/DATA101

Mach, D. M., Blakeslee, R. J., Bateman, M. G., & Bailey, J. C. (2009). Electric fields, conductivity, and estimated currents from aircraft overflights of electrified clouds. *Journal of Geophysical Research*, *114*(D10), D10204. https://doi.org/10.1029/2008JD011495

Mach, D. M., & Koshak, W. J. (2007). General matrix inversion technique for the calibration of electric field sensor arrays on aircraft platforms. *Journal of Atmospheric and Oceanic Technology*, *24*(9), 1576–1587. https://doi.org/10.1175/JTECH2080.1

Mansell, E. R., MacGorman, D. R., Ziegler, C. L., & Straka, J. M. (2005). Charge structure and lightning sensitivity in a simulated multicell thunderstorm. *Journal of Geophysical Research*, *110*(D12), D12101. https://doi.org/10.1029/2004JD005287

Mansell, E. R., Ziegler, C. L., & Bruning, E. C. (2010). Simulated electrification of a small thunderstorm with two-moment bulk microphysics. *Journal of the Atmospheric Sciences*, *67*(1), 171–194. https://doi.org/10.1175/2009JAS2965.1

Market, P. S., & Becker, A. E. (2009). A study of lightning flashes attending periods of banded snowfall. *Geophysical Research Letters*, *36*(1), L01809. https://doi.org/10.1029/2008GL036317

Market, P. S., Halcomb, C. E., & Ebert, R. L. (2002). A climatology of thundersnow events over the contiguous United States. *Weather and Forecasting*, *17*(6), 1290–1295. https://doi.org/10.1175/1520-0434(2002)017<1290:ACOTEO>2.0.CO;2

Market, P. S., Oravetz, A. M., Gaede, D., Bookbinder, E., Lupo, A. R., Melick, C. J., et al. (2006). Proximity soundings of thundersnow in the central United States. *Journal of Geophysical Research*, *111*(D19), D19208. https://doi.org/10.1029/2006JD007061

McMurdie, L., Heymsfield, G., Yorks, J. E., & Braun, S. A. (2019). Investigation of microphysics and precipitation for Atlantic coast-threatening snowstorms (IMPACTS) collection [Dataset]. NASA EOSDIS Global Hydrometeorology Resource Center Distribution Active Archive Center. https://doi.org/10.5067/IMPACTS/DATA101

McMurdie, L. A., Heymsfield, G. M., Yorks, J. E., Braun, S. A., Skofronick-Jackson, G., Rauber, R. M., et al. (2022). Chasing snowstorms: The investigation of microphysics and precipitation for Atlantic coast-threatening snowstorms (IMPACTS) campaign. *Bulletin of the American Meteorological Society*, *103*(5), E1243–E1269. https://doi.org/10.1175/BAMS-D-20-0246.1

Mitchell, D. L. (1996). Use of mass- and area-dimensional power laws for determining precipitation particle terminal velocities. *Journal of the Atmospheric Sciences*, *53*(12), 1710–1723. https://doi.org/10.1175/1520-0469(1996)053<1710:UOMAAD>2.0.CO;2

Peters-Lidard, C. D., Kemp, E. M., Matsui, T., Santanello, J. A., Kumar, S. V., Jacob, J. P., et al. (2015). Integrated modeling of aerosol, cloud, precipitation and land processes at satellite-resolved scales. *Environmental Modelling and Software*, *67*, 149–159. https://doi.org/10.1016/j.envsoft.2015.01.007

Pruppacher, H. R., & Klett, J. D. (1978). *Microphysics of clouds and precipitation* (Vol. 18). Kluwer Academic Publishers.

Rauber, R. M., Wegman, J., Plummer, D. M., Rosenow, A. A., Peterson, M., McFarquhar, G. M., et al. (2014). Stability and charging characteristics of the comma head region of continental winter cyclones. *Journal of the Atmospheric Sciences*, *71*(5), 1559–1582. https://doi.org/10.1175/JAS-D-13-0253.1

Reynolds, S. E., Brook, M., & Gourley, M. F. (1957). Thunderstorm charge separation. *Journal of the Atmospheric Sciences*, *14*(5), 426–436. https://doi.org/10.1175/1520-0469(1957)014<0426:TCS>2.0.CO;2

Rogers, R. R., & Yau, M. K. (1989). *A Short course in cloud physics*. Pergamon Press.

Rust, W. D., & Trapp, R. J. (2002). Initial balloon soundings of the electric field in winter nimbostratus clouds in the USA. *Geophysical Research Letters*, *29*(20), 20-1–20-4. https://doi.org/10.1029/2002GL015278

Saunders, C. P. R., Bax-norman, H., Emersic, C., Avila, E. E., & Castellano, N. E. (2006). Laboratory studies of the effect of cloud conditions on graupel/crystal charge transfer in thunderstorm electrification. *Quarterly Journal of the Royal Meteorological Society*, *132*(621), 2653–2673. https://doi.org/10.1256/qj.05.218

Saunders, C. P. R., & Peck, S. L. (1998). Laboratory studies of the influence of the rime accretion rate on charge transfer during crystal/graupel collisions. *Journal of Geophysical Research*, *103*(D12), 13949–13956. https://doi.org/10.1029/97JD02644

Saunders, C. P. R., Peck, S. L., Aguirre Varela, G. G., Avila, E. E., & Castellano, N. E. (2001). A laboratory study of the influence of water vapour and mixing on the charge transfer process during collisions between ice crystals and graupel. *Atmospheric Research*, *58*(3), 187–203. https://doi.org/10.1016/S0169-8095(01)00090-4

Schultz, C. J., Harkema, S. S., Mach, D. M., Bateman, M., Lang, T. J., Heymsfield, G. M., et al. (2021). Remote sensing of electric fields observed within winter precipitation during the 2020 Investigation of Microphysics and Precipitation for Atlantic Coast-Threatening Snowstorms (IMPACTS) field campaign. *Journal of Geophysical Research: Atmospheres*, *126*(16), e2021JD034704. https://doi.org/10.1029/2021JD034704

Schultz, C. J., Lang, T. J., Bruning, E. C., Calhoun, K. M., Harkema, S., & Curtis, N. (2018). Characteristics of lightning within electrified snowfall events using lightning mapping arrays. *Journal of Geophysical Research: Atmospheres*, *123*(4), 2347–2367. https://doi.org/10.1002/2017JD027821

Schultz, D. M. (1999). Lake-effect snowstorms in northern Utah and western New York with and without lightning. *Weather and Forecasting*, *14*(6), 1023–1031. https://doi.org/10.1175/1520-0434(1999)014<1023:LESINU>2.0.CO;2

Skamarock, W., & Klemp, J. (2008). A time-split nonhydrostatic atmospheric model for weather research and forecasting applications. *Journal of Computational Physics*, *227*(7), 3465–3485. https://doi.org/10.1016/j.jcp.2007.01.037

Takahashi, T. (1978). Riming electrification as a charge generation mechanism in thunderstorms. *Journal of the Atmospheric Sciences*, *35*(8), 1536–1548. https://doi.org/10.1175/1520-0469(1978)035<1536:REAACG>2.0.CO;2

Takahashi, T., Endoh, T., Wakahama, G., & Fukuta, N. (1991). Vapor diffusional growth of free-falling snow crystals between -3 and -23°C. *Journal of the Meteorological Society of Japan. Ser. II*, *69*(1), 15–30. https://doi.org/10.2151/jmsj1965.69.1_15

Takahashi, T., & Fukuta, N. (1988). Supercooled cloud tunnel studies on the growth of snow crystals between-4 and-20°C. *Journal of the Meteorological Society of Japan. Ser. II*, *66*(6), 841–855. https://doi.org/10.2151/jmsj1965.66.6_841

Takahashi, T., Tajiri, T., & Sonoi, Y. (1999). Charges on graupel and snow crystals and the electrical structure of winter thunderstorms. *Journal of the Atmospheric Sciences*, *56*(11), 1561–1578. https://doi.org/10.1175/1520-0469(1999)056<1561:COGASC>2.0.CO;2

Takeuti, T., Nakano, M., Brook, M., Raymond, D. J., & Krehbiel, P. (1978). The anomalous winter thunderstorms of the Hokuriku Coast. *Journal of Geophysical Research*, *83*(C5), 2385–2394. https://doi.org/10.1029/JC083iC05p02385

Williams, E. R. (1985). Large-scale charge separation in thunderclouds. *Journal of Geophysical Research*, *90*(D4), 6013–6025. https://doi.org/10.1029/JD090iD04p06013

Williams, E. R., & Lhermitte, R. M. (1983). Radar tests of the precipitation hypothesis for thunderstorm electrification. *Journal of Geophysical Research*, *88*(C15), 10984–10992. https://doi.org/10.1029/JC088iC15p10984

Zheng, D., Wang, D., Zhang, Y., Wu, T., & Takagi, N. (2019). Charge regions indicated by LMA lightning flashes in Hokuriku's winter thunderstorms. *Journal of Geophysical Research: Atmospheres*, *124*(13), 7179–7206. https://doi.org/10.1029/2018JD030060

Ziegler, C. L., & MacGorman, D. R. (1994). Observed lightning morphology relative to modeled Space charge and electric field distributions in a tornadic storm. *Journal of the Atmospheric Sciences*, *51*(6), 833–851. https://doi.org/10.1175/1520-0469(1994)051<0833:OLMRTM>2.0.CO;2

Ziegler, C. L., MacGorman, D. R., Dye, J. E., & Ray, P. S. (1991). A model evaluation of noninductive graupel-ice charging in the early electrification of a mountain thunderstorm. *Journal of Geophysical Research*, *96*(D7), 12833–12855. https://doi.org/10.1029/91JD01246